Numerical Simulations of Inviscid Air-Flows through the Ramjet Inlets

M. Akbarzadeh M. J. Kermani
Department of Mechanical Engineering
Amirkabir University of Technology (Tehran Polytechnic)
Tehran, Iran, 15875-4413
Contact: mkermani@ aut.ac.ir

Abstract

The performances of three different ramjet inlets (Inlets 1 to 3) and one entire ramjet are numerically studied in this paper. The fluid is assumed to be inviscid. Inlet 1 is a supersonic inlet (suitable for supersonic combustion ramjets, scramjets) and is chosen from the literature to validate the results of the present computations. Inlets 2 and 3 are instead designed in the present study based on the Oswatitsch principle. Inlets 2 and 3 produce a series of oblique shocks merging at the cowl lip of the engine, which are followed by a terminating normal shock located at downstream of the inlet throat. Also in this paper computations are performed for an entire ramjet engine. The designed ramjet inlet gives two oblique shocks + one terminating normal shock with a satisfactory pressure recovery. The effect of combustion in the ramjet is modelled using a volumetric heat source function distributed throughout the combustion chamber. The position of terminating normal shock in Inlets 2 and 3 are controlled by the inlet's back pressure. However, in the ramjet the position of normal shock in the inlet-diffuser is influenced by the heat rate added through the ramjet's combustion chamber, and the exhaust nozzle throat area. Detailed information about the performance of the inlets and the entire ramjet engine are provided in the paper.

For the numerical simulations, the inviscid flux difference splitting scheme of Roe (1981) with various spatial orders of accuracy (including the third-order upwind biased algorithm) and the predictor-corrector scheme of MacCormack (1969) are implemented in this study. The van Albada flux limiter (1982) is used to prevent spurious numerical oscillations in high resolution computations using the Roe scheme, while the artificial viscosity terms are added to the MacCormack scheme to damp the unwanted numerical oscillations. The commercial software package of Fluent has also been used in some cases to double check the accuracy of the computation. The computations of the supersonic inlet (Inlet 1) are compared with those reported in the literature [8]. All comparisons show very good agreement.

Keywords: Supersonic-Subsonic Inlet-diffusers, Ramjets, Roe Scheme, MacCormack Scheme

1 Introduction

Ramjet engines are very promising devices for supersonic air–breathing vehicles. These engines are mechanically much simpler than turbojet types, while they can operate more efficiently at supersonic speeds.

However, the design of these engines encounter some problems as they are expected to cover flights at various operating conditions. Ramjet engines consist of (1) an inlet diffuser (either conical- or wedge shaped-center body), (2) an integrated combustion chamber and (3) an exhaust nozzle. The compression process is carried out by the inlet-diffuser that is followed by the combustion chamber. At last, in the exhaust nozzle, the potential energy of the hot and compressed gases converts to kinetic energy to provide the required thrust for the engine [1].

The role of engine inlet is very vital for all air-breathing propulsion systems; especially for ramjets in which all the compression process is performed by its own. This is as opposed to, say, turbojets that contain compressors to enhance the compression processes.

A ramjet inlet is supposed to perform the following tasks: (1) collect the atmospheric air at the designed supersonic speed (generally it is expected the inlet do this task at any free stream Mach number and any flight altitude during the wide spectrum of the ramjet flight), (2) slow it down through a series of oblique shocks followed by a terminating normal shock (generally this involves a change in the flow direction as the flow usually passes through a series of oblique shocks), and (3) deliver the compressed air flow to the ramjet combustion chamber at Mach number of about $M_{cc} \approx 0.5$, where M_{cc} is the Mach number at the combustion chamber entrance face (generally $M_{cc} = 0.5$ is a suitable Mach number for subsonic combustors in order to give stabilized combustion processes). In addition, the inlet is expected to deliver the compressed air-flow to the combustion chamber at an acceptable level of uniformity of the pressure and speed. These are to assure stable combustion processes in the ramjet combustion chambers. These tasks, as noted earlier, should be done under any flight condition. Finally, the inlet should achieve all of these with (a) minimum external drag and disturbance to the external flows around it, and (b) at highest possible pressure recovery (i.e. highest inlet efficiency). As the ramjet inlet is the –one man show component– to do the compression process (as opposed to, say, turbojets which contain compressors as well), so its appropriate performance is highly important. In this role, the inlet is considered an essential part of the engine cycle and its efficiency is directly translated to the engine performance.

The supersonic inlet consists of a spike (center-body or fore-body) and an integrated duct. The initial compression is done by the spike. When designing a supersonic inlet, an increase in the flight Mach number requires the increase in the oblique shock numbers in order to save total pressure recovery. Therefore, the principle of staging a supersonic compression like the Oswatitsch principle is used to reduce the inlet losses in a most efficient manner.

The combined-compression process takes place via multiple shock waves generated by the external-compression surfaces and the cowl, and later by the internal-compression surfaces from the cowl lip toward the inner part of the engine face [2, 3].

Most of the computations reported in the literature are for supersonic combustion chamber inlets, scramjet inlets [4, 5, 6]. The geometry of these inlets are not very complicated as the flow in these inlets lack any normal shock. On the other hand the flow field through the ramjet inlets passes through several oblique

shocks then it is converted to subsonic flow through a terminating normal shock. In the following the flow is delivered to the combustion chamber. Ramjet inlets are much more complicated due to the formation of a terminal normal shock. Combustion processes are introduced to the ramjet inlets using an elevated back pressure [7]. The problem definition is given in the following.

1.1 Problem Definition

In this paper three different ramjet inlets and one entire ramjet are numerically studied. The flow is assumed to be inviscid. Viscous turbulent computations are underway and will come in a separate study. Inlet 1 is a supersonic inlet (suitable for scramjets), and is chosen from the literature [8] for validating the results of the present computations.

The supersonic portions of Inlet 2 and 3 are designed based on the Oswatitsch principle [2] in the present study. Inlet 2 gives three oblique shocks in the external portion of the inlet. The flow turning through these oblique shocks are very high hence the inlet produces a very high amount of cowl drag as compared to Inlet 3. The supersonic flow then enters the internal portion of Inlet 2, and passes through a terminating normal shock following the inlet throat. This post shock subsonic flow continues its motion through the divergent portion of the inlet until the flow is delivered to the combustion chamber at Mach number of about 0.5. Inlet 3, instead, gives two external oblique shocks + one internal oblique shock followed by a terminating normals shock. Similar to Inlet 2, the subsonic flow further diffuses through the diffuser of Inlet 3, and the flow is delivered to the combustion chamber at Mach number of about 0.5 again. Also in the present study computations are performed for an entire ramjet engine. The effect of combustion through the ramjet combustion chamber is modelled by distributing a simple but realistic volumetric heat source (VHS).

The position of normal shock in Inlets 2 and 3 are controlled by the inlet back pressures. For the entire ramjet, as no boundary condition is imposed at the entrance face of the combustion chamber, the position of normal shock is fixed by (1) the rate of heat release ($Watts$) through the combustion chamber, and the exhaust nozzle throat area. A set of parametric studies are performed on the effects of VHS and the exhaust nozzle throat area on the position of normal shock. The dependence of cowl drag (the pressure drag), thrust and thrust specific fuel consumption (TSFC) on the geometrical and operational parameters are discussed in the present paper.

The numerical simulations are performed using the flux difference splitting scheme of Roe [9] with various spatial orders of accuracy (including the third-order upwind biased algorithm) and the predictor-corrector scheme of MacCormack [10]. The Roe scheme is an Approximate Riemann Solver (ARS), so is computationally much more efficient than the Exact Riemann Solvers (ERS) used in Godunov type schemes. These features of the Roe scheme have made it one of the most popular density-based schemes for compressible flows. The spurious numerical oscillations in high resolution computations using the Roe scheme are damped by van Albada flux limiter (1982), while the artificial viscosity terms are added to the MacCormack scheme to damp the unwanted numerical oscillations. The commercial software package of Fluent

has also been used in few cases to double check the accuracy of the computation. The computations of the supersonic inlet (Inlet 1) are compared with those reported in the literature [8]. All comparisons show very good agreement.

2 Governing Equations

The governing equations are solved in generalized coordinates in the present study. The fluid is assumed to be inviscid. The equations for the inviscid, unsteady and compressible flow in full conservative form and in generalized coordinates with no body force for both planar and axisymmetric cases are shown by: (see Refs. [11, 12] for example)

$$\frac{\partial Q_1}{\partial t} + \frac{\partial F_1}{\partial \xi} + \frac{\partial G_1}{\partial \eta} + \alpha H_1 = 0 \tag{1}$$

where Q_1 is the conservative vector, F_1 and G_1 are respectively the inviscid flux vectors in ξ- and η-directions, and H_1 is the axisymmetric space term in generalized coordinates. In Eqn. 1 $\alpha = 0$ corresponds to the planar case and $\alpha = 1$ to axisymmetric flow condition. The conservative and flux vector term in generalized coordinate are connected to those in physical space using,

$$\begin{aligned} Q_1 &\equiv JQ, \\ F_1 &\equiv J\left(\xi_x F + \xi_y G\right), \\ G_1 &\equiv J\left(\eta_x F + \eta_y G\right), \\ H_1 &\equiv JH, \end{aligned} \tag{2}$$

where ξ_x, ξ_y, η_x, η_y, and J are respectively the metrics and Jacobian of transformation, and:

$$Q = \begin{bmatrix} \rho \\ \rho u \\ \rho v \\ \rho e_t \end{bmatrix}, \qquad F = \begin{bmatrix} \rho u \\ \rho u^2 + p \\ \rho uv \\ \rho u h_t \end{bmatrix}, \qquad G = \begin{bmatrix} \rho v \\ \rho uv \\ \rho v^2 + p \\ \rho v h_t \end{bmatrix}, \qquad H = \frac{1}{y}\begin{bmatrix} \rho v \\ \rho uv \\ \rho v^2 \\ \rho v h_t \end{bmatrix}.$$

Here, ρ is the density, u and v are respectively the x and y velocity components, e_t is the total energy, p is the static pressure, and h_t is the total enthalpy. In the present study, for the air as ideal gas, the equation of state:

$$p = \rho RT, \tag{3}$$

is used, wherein R ($= 287.0\ J/kg.K$ for air) is the gas constant. The internal energy, e, is determined assuming a constant value for the specific heat at constant volume,

$$e = c_v T, \tag{4}$$

where $c_v = R/(\gamma - 1)$, with $\gamma = 1.4$ for the air.

3 Time Discretization

For the Roe scheme used in the present study, the following two-step predictor-corrector explicit time integration from the Lax-Wendroff family is used [13]. The predictor step provides the flow condition in an intermediate step $n+1/2$.

$$\frac{Q_1^{n+1/2}-Q_1^n}{\Delta t/2} \quad + \quad \left(\frac{\partial F_1}{\partial \xi}\right)^n + \left(\frac{\partial G_1}{\partial \eta}\right)^n + \alpha H_1^n = 0 \tag{5}$$

Eqn. 5 gives $Q_1^{n+1/2}$, from which all the primitive variables at the time step $n+1/2$ can be determined. The predictor step is followed by the corrector step, which completes the integration. In the corrector step, a central differencing in time around $n+1/2$ is implemented as follows:

$$\frac{Q_1^{n+1}-Q_1^n}{\Delta t} \quad + \quad \left(\frac{\partial F_1}{\partial \xi}\right)^{n+1/2} + \left(\frac{\partial G_1}{\partial \eta}\right)^{n+1/2} + \alpha H_1^{n+1/2} = 0\,. \tag{6}$$

4 Space Discretization

For the spatial discretization of the Roe scheme the inner (L) and outer (R) (see Fig. 1) flow conditions are determined using either the first-, second-, and third-order upwind biased algorithm. The MUSCL strategy, [14], is used to extrapolate the primitive variables pressure (p), velocity components (u, v) and temperature (T) to the cell faces.

For example at the east face of the control volume (E) the L and R flow conditions are determined as follows:

$$\begin{aligned} q_E^L &= q_{i,j} + \frac{1}{4}[(1-\kappa)\Delta_W q + (1+\kappa)\Delta_E q], \\ q_E^R &= q_{i+1,j} - \frac{1}{4}[(1-\kappa)\Delta_{EE} q + (1+\kappa)\Delta_E q]. \end{aligned} \tag{7}$$

where q represents either of the four primitive variables, i.e. $q \in \{p, u, v, T\}$, $\kappa = -1$ and $1/3$ correspond, respectively, to the second order upwind and the third order upwind-biased algorithms. For the first order algorithm the L and R side values of the primitive variables at the E-face (see Fig. 1) are determined from: $q_E^L = q_{i,j}$ and $q_E^R = q_{i+1,j}$. In Eqn. 7, $\Delta_W q$, $\Delta_E q$ and $\Delta_{EE} q$ are the jumps of the primitive variables at the cell faces, i.e. $\Delta_W q = q_{i,j} - q_{i-1,j}$, $\Delta_E q = q_{i+1,j} - q_{i,j}$ and $\Delta_{EE} q = q_{i+2,j} - q_{i+1,j}$. A similar formula can be written for the inner (L) and outer (R) q values at the north face of the control volume (i.e. q_N^L and q_N^R) shown in Fig. 1.

To damp the spurious numerical oscillation in high resolution computations (i.e. in the second and third order extrapolations), the van Albada flux limiter (1982) is applied. This limits the slope of extrapolation,

$$\begin{aligned} q_E^L &= q_{i,j} + \frac{\phi}{4}[(1-\kappa)\Delta_W q + (1+\kappa)\Delta_E q] \\ q_E^R &= q_{i+1,j} - \frac{\phi}{4}[(1-\kappa)\Delta_{EE} q + (1+\kappa)\Delta_E q]. \end{aligned} \tag{8}$$

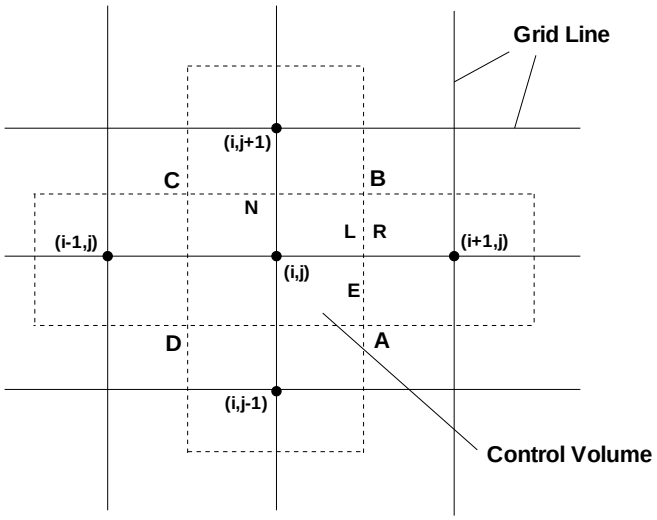

Figure 1: Configuration of grids with the inner (L) and outer (R) values for the cell (i,j). Grid lines are shown by solid lines and control volume boundaries with dashed-lines [12].

where ϕ is the limiter function defined by:

$$\phi_{i,j} \equiv \frac{2(\Delta_W q)(\Delta_E q) + \varepsilon_0}{(\Delta_W q)^2 + (\Delta_E q)^2 + \varepsilon_0} \tag{9}$$

and ε_0 is a small number which prevents indeterminacy in regions of uniform flow, i.e. in and around $\Delta_W q = \Delta_E q = 0$.

To avoid expansion shocks in the regions that the eigenvalues vanish, a formerly developed entropy correction formula [15], is used throughout this paper,

$$\begin{cases} \hat{\lambda}_{new} \leftarrow \left(\hat{\lambda}^2 + \varepsilon^2\right)/2\varepsilon \qquad |\lambda| < \varepsilon \\ \\ \varepsilon = 4.0 \; max\left[0, \left(\hat{\lambda} - \lambda^L\right), \left(\lambda^R - \hat{\lambda}\right)\right], \end{cases} \tag{10}$$

where $\hat{\lambda}$ is the eigenvalue of the Jacobian flux matrix determined at Roe's averaged condition, and λ^L and λ^R are the eigenvalues determined at the inner and outer flow conditions, respectively.

4.1 The Numerical Flux Roe

The numerical flux Roe is obtained based on the formerly developed formulae [12, 16]:

$$\text{East Face} : F_E = \frac{1}{2}\left(F_E^L + F_E^R\right) - \frac{1}{2}\sum_{k=1}^{4} |\hat{\lambda}_E^{(k)}| \; \delta w_E^{(k)} \; \hat{T}_E^{(k)} \tag{11}$$

$$\text{North Face} : G_N = \frac{1}{2}\left(G_N^L + G_N^R\right) - \frac{1}{2}\sum_{k=1}^{4} |\hat{\lambda}_N^{(k)}| \; \delta w_N^{(k)} \; \hat{T}_N^{(k)} \tag{12}$$

where λ is the eigenvalue of the Jacobian flux matrix, T is the corresponding eigenvector, and δw is the wave amplitude vector.

4.2 Roe's Averaging

The numerical flux for the Roe scheme is calculated at the so-called Roe-averaged values [9], which are obtained from the inner L and outer R state values at the sides of, say, E cell face:

$$\hat{\rho}_{_E} = \sqrt{\rho_{_E}^{L}\ \rho_{_E}^{R}} \tag{13}$$

$$\hat{u}_{_E} = \frac{\sqrt{\rho_{_E}^{L}}u_{_E}^{^L} + \sqrt{\rho_{_E}^{R}}u_{_E}^{^R}}{\sqrt{\rho_{_E}^{L}} + \sqrt{\rho_{_E}^{R}}} \tag{14}$$

$$\hat{v}_{_E} = \frac{\sqrt{\rho_{_E}^{L}}v_{_E}^{^L} + \sqrt{\rho_{_E}^{R}}v_{_E}^{^R}}{\sqrt{\rho_{_E}^{L}} + \sqrt{\rho_{_E}^{R}}} \tag{15}$$

$$\hat{h_t}_{_E} = \frac{\sqrt{\rho_{_E}^{L}}h_{t_{_E}}^{^L} + \sqrt{\rho_{_E}^{R}}h_{t_{_E}}^{^R}}{\sqrt{\rho_{_E}^{L}} + \sqrt{\rho_{_E}^{R}}} \tag{16}$$

A similar formula cab be written for the quantities on the north side of a cell face ($\hat{\rho}_{_N}$, $\hat{u}_{_N}$, etc.).

5 MacCormack Scheme

In the present study, the governing equations for some cases are also solved using the predictor-corrector scheme of MacCormack, detailed for example in [10]. This predictor-corrector scheme is of second-order accuracy both in space and time:

$$\text{Predictor Step} : \bar{Q}_{1_{i,j}}^{n+1} = Q_{1_{i,j}}^{n} - \Delta t\left[\frac{\left(F_{1_{i+1,j}}^{n} - F_{1_{i,j}}^{n}\right)}{\Delta\xi} + \frac{\left(G_{1_{i,j+1}}^{n} - G_{1_{i,j}}^{n}\right)}{\Delta\eta} + H_{1_{i,j}}^{n}\right] \tag{17}$$

$$\text{Corrector Step} : Q_{1_{i,j}}^{n+1} = \frac{1}{2}\left(Q_{1_{i,j}}^{n} + \bar{Q}_{1_{i,j}}^{n+1}\right) - \frac{\Delta t}{2}\times \left[\frac{\left(\bar{F}_{1_{i,j}}^{n+1} - \bar{F}_{1_{i-1,j}}^{n+1}\right)}{\Delta\xi} + \frac{\left(\bar{G}_{1_{i,j}}^{n+1} - \bar{G}_{1_{i,j-1}}^{n+1}\right)}{\Delta\eta} + \bar{H}_{1_{i,j}}^{n+1}\right] \tag{18}$$

Here, the forward differences are used for all spatial derivatives in the predictor step, followed by the backward differences in the corrector step. These give the net scheme to be spatially second order. As the forward and backward differences are alternated between the predictor and corrector steps, this eliminates any bias due to the one-sided differentiation [6]. However, the alternation in the order of spatial differentiation introduces a pseudo-unsteadiness to the solution when marched in time. Therefore, the MacCormack scheme cannot reach to machine accuracy [17].

For the MacCormack scheme in regions with large discontinuities such as shocks, an artificial viscosity term (AV) is added to stabilize the solution. To do so, in the present study, a fourth-order dissipation term,

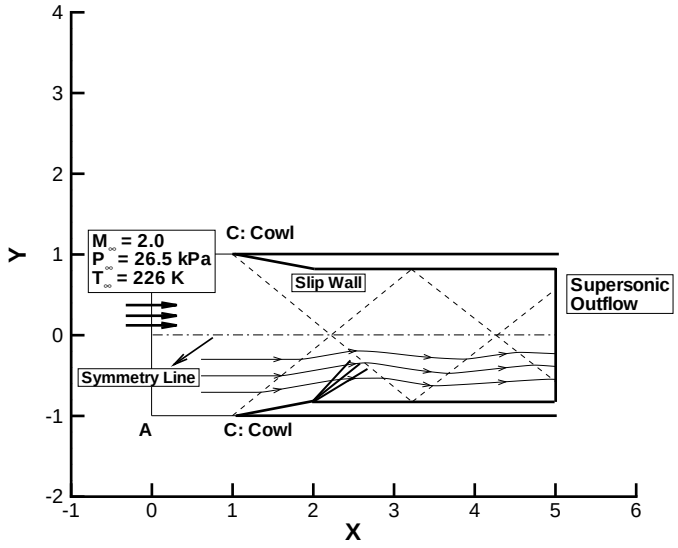

Figure 2: Geometry and boundary conditions for Inlet 1 (all dimensions in meter).

with two adjustable constants C_x and C_y, are employed. These terms are added to the right-hand side of predictor and corrector steps. The artificial viscosity term (AV) at the (i, j) node is given by [10]:

$$\begin{aligned} AV_{i,j} &= C_x \frac{|p_{i+1,j} - 2p_{i,j} + p_{i-1,j}|}{p_{i+1,j} + 2p_{i,j} + p_{i-1,j}} \left(Q_{1_{i+1,j}} - 2Q_{1i,j} + Q_{1i-1,j} \right) \\ &+ C_y \frac{|p_{i,j+1} - 2p_{i,j} + p_{i,j-1}|}{p_{i,j+1} + 2p_{i,j} + p_{i,j-1}} \left(Q_{1_{i,j+1}} - 2Q_{1i,j} + Q_{1i,j-1} \right) \end{aligned} \tag{19}$$

where C_x and C_y in Eqn. 19, are the adjustable constants which are in the range of 0 to 0.5. In the present study, we have chosen $C_x = C_y = 0.1$.

6 Geometries and Boundary Conditions

6.1 Inlet 1; Supersonic Flow to the Combustion Chamber

Inlet 1 chosen from the literature [8], is a supersonic inlet, and is suitable for supersonic combustion ramjets (scramjets). It is considered for validating the results of the present computations. The inlet is a multi-oblique-shock supersonic inlet that delivers the air flow at supersonic speeds to the combustion chamber. The geometrical dimensions of the inlet, the computational domain, and the boundary conditions are depicted in Fig. 2. The compression corner shown in the figure is 10-degrees.

For the boundary conditions, supersonic flow at flight Mach = 2, and altitude $\approx 10\ km$ ($p_\infty = 26.5\ kPa$ and $T_\infty = 226\ K$) enters to the computational domain. At the exit, for the supersonic outflow all the flow parameters of p, T, u, and v are extrapolated from the internal nodes. The line AC (a line extended from the leading edge of the cowl to the computational domain inlet plane) is assumed to be a straight streamline. This is a totally true assumption for the supersonic approaching flow. Therefore, the vertical component of velocity is set to zero along this line. Due to the symmetry conditions along the centerline, only one side of the centerline is computed here, along which the symmetry conditions are applied. Along the surface of the wall, no-penetration through the solid wall is permitted, i.e. $\vec{V} \cdot \hat{n} = 0$.

6.2 The Oswatitsch Principle

The design of the supersonic portion of Inlets 2 and 3 are performed using the Oswatitsch principle. The principle states that for a two-dimensional supersonic duct, the maximum shock-pressure-recovery can be obtained if the strength of train of oblique shocks are equal [2]. That is, the components of Mach numbers in directions normal to the shocks are equal (see Fig. 3),

$$M_1 \sin\beta_1 = M_2 \sin\beta_2 = M_3 \sin\beta_3 = ... = M_{n-1} \sin\beta_{n-1} \tag{20}$$

where n is the number of shock waves ($n-1$ oblique shocks + one terminating normal shock) and M_i ($1 \leq i \leq n-1$) is the Mach number upstream of the ith shock, and β is the shock angle, as shown in Fig. 3. In Eqn. 20, $M_i \sin\beta_i$ (= M_{n_i}) is the component of Mach number normal to the ith shock. In fact Eqn. 20 implies that M_{n_i} remains constant throughout the train of oblique shocks for minimized shock losses. Inlets 2 and 3 (see Sections 6.3 and 6.4 for detail) are ramjet inlets which their supersonic portions are designed based on the Oswatitsch principle. A ramjet inlet receives supersonic airstream, and decelerates the flow through a train of oblique shocks followed by a terminating normal shock, then delivers the flow to the combustion chamber at subsonic speeds. In the following, two ramjet inlets (Inlets 2 and 3) are explained. Inlet 2 performs the supersonic compression processes solely through the external portion of the inlet, while Inlet 3, does this task through the combined internal and external portions of the inlet.

6.3 Inlet 2; External Compression

Inlet 2 is designed based on the Oswatitsch principle (see Section 6.2 for detail). The inlet receives flow at Mach = 2.5, and is designed to give the supersonic compression solely in the external portion of the inlet. The inlet is of planar geometry with shocks focused at its cowl lip.

According to the Oswatitsch principle, for the optimum supersonic compression, the component of Mach numbers normal to the train of shocks should be same. This leads to ramp angles of $\delta_1 = 9.5^\circ$, $\delta_2 = 10.5^\circ$ and $\delta_3 = 11.5^\circ$ (see Table 1). These flow turning angles (δ_1 to δ_3) determines the Mach number upstream of the terminating normal shock, i.e. M_4 = 1.30. The results of the calculations are summarized in Table 1.

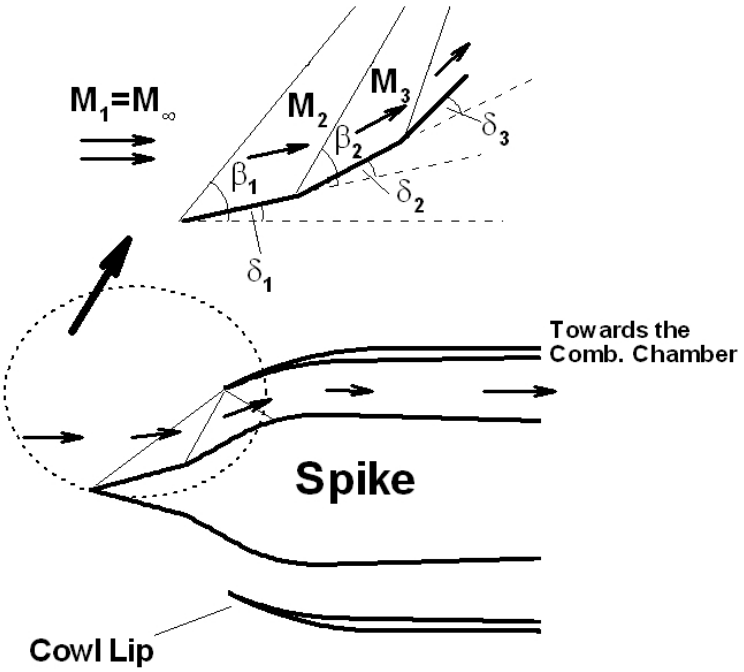

Figure 3: Shock angles β and flow turning angles δ for a typical supersonic inlet.

Table 1: Flow turning angles, the corresponding shock wave angles, and the Mach number sequences for Inlet 2

$\delta_1 = 9.5°$	$\beta_1 = 31.38°$	$M_2 = 2.11$	$M_1 \sin\beta_1 = 1.30$
$\delta_2 = 10.5°$	$\beta_2 = 37.84°$	$M_3 = 1.72$	$M_2 \sin\beta_2 = 1.29$
$\delta_3 = 11.5°$	$\beta_3 = 48.63°$	$M_4 = 1.30$	$M_3 \sin\beta_3 = 1.29$

As shown in this table, the value of $M_i \sin\beta_i = M_{n_i}$ is within the range of $(1.29, 1.30)$, so M_{n_i} is almost constant. That is, the Oswatitsch principle is fairly regarded.

For an inlet, the captured airflow (or airstream) is determined from the spacing between the engine centerline and the so-called bounding streamline. This spacing is shown by $A_\infty/2$ in Fig. 4. Here the bounding streamline is a streamline (or streamtube in axial cases) originated from the engine cowl and extended to freestream, as shown in Fig. 4. Hence, the location of cowl lip is determined from the intersection of the first shock with the bounding streamline, see Fig. 4. This fixes the spike apex angle δ_1 (see Fig. 4 or Table 1). With $M_1 = 2.5$, and δ_1 and β_1 values given in Table 1, the post shock Mach number is obtained as $M_2 = 2.11$. Also with known turning angle $\delta_2 = 10.5°$, the ramp location of the second oblique shock that will merge the first shock at the cowl lip can be determined. The same procedure can be repeated until the last shock. Complete information including the flow turning angles for Inlet 2 is given in Table 1.

The geometry and boundary conditions for Inlet 2 are shown in Fig. 5. For the supersonic inflow and

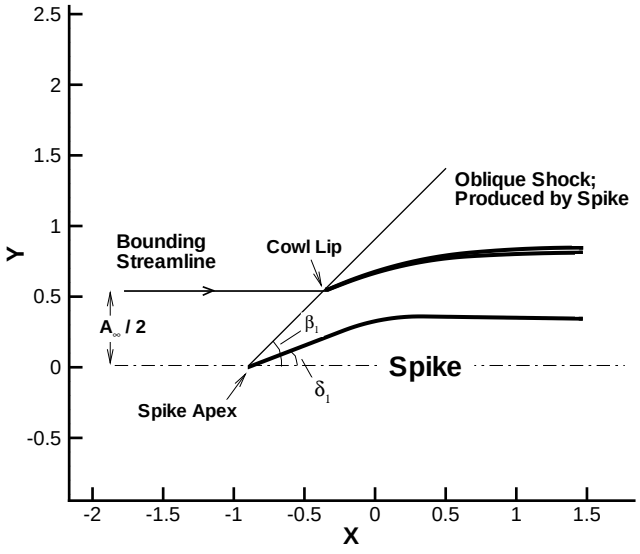

Figure 4: The configuration of the cowl lip position and the bounding streamline.

outflow, the boundary conditions are exactly similar to those of the Inlet 1. For the subsonic outflow (where the flow is delivered to the engine combustion chamber) the back pressure is specified, and other three parameters T, u, and v are extrapolated from the interior nodes.

6.4 Inlet 3; Combined Internal and External Compression

In the case of Inlet 2, in which the compression process is solely performed in the external portion of the inlet, the outward turning of flow (i.e. diversion of flow away from the engine centerline) due to the train of oblique shocks requires the inlet cowl to highly bend inward (i.e. turn toward the centerline). This bent of the cowl lip significantly raises the engine pressure drag, and is called the cowl drag. Alternatively combined compression, i.e. supersonic compressions in both external and internal portions of the inlet, is used to reduce the cowl drag.

The schematic of Inlet 3 that posses combined internal and external compression is illustrated in Fig. 6. Here the first two compression processes are performed in the external portion of the inlet, and give 20° total turn. That is, 9.5° flow turning by Ramp 1 + 10.5° flow turning by Ramp 2 (see Fig. 6). These shocks are focused at the cowl lip, where an inward bend (turning toward the centerline) angle of 11.5° is made at the cowl lip. On the surface of the spike, Ramp 2 is continued just before it meets the reflected shock from the cowl lip. An inward diversion of the spike surface (turning toward the centerline) at the intersection point eliminates the shock reflection and allows the normal shock to be formed due to the elevated back pressure.

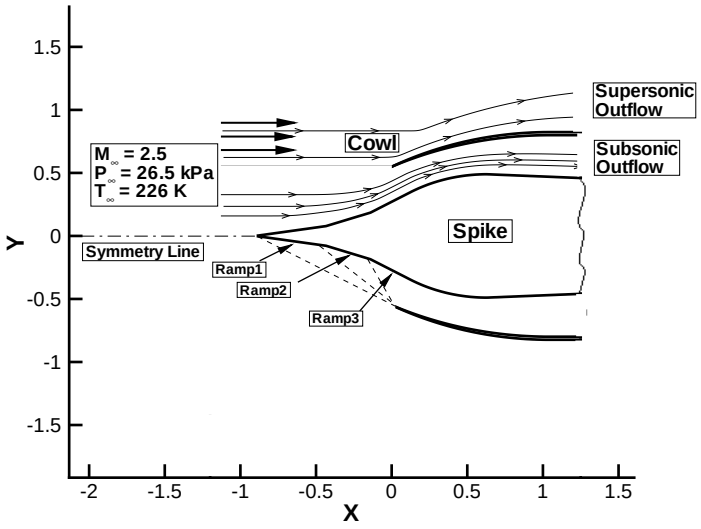

Figure 5: Geometry and boundary conditions for Inlet 2 giving external compression solely (all dimensions in meter).

The boundary conditions specified for Inlet 3 are identical to those of Inlet 2.

6.5 Grid Configurations

In this study, the computational domain is divided into two subdomains (except for Inlet 1 which has a single computational domain), and an algebraic method is employed to generate structured quadrilateral grids, [20, 21], in each subdomain. Fig. 7 shows sample of grid configurations for Subdomains 1 and 2 for Inlet 3.

To determine adequate grid sizes for each geometry, grid independency check are conducted in the present study. A sample of results that shows the variation of pressure coefficient C_p along the spike surface of Inlet 3 with various grid sizes are shown in Fig. 8, where:

$$C_p = \frac{p - p_\infty}{1/2\ \rho_\infty V_\infty^2}. \tag{21}$$

The grid sizes for grid independent computations and for all the geometries used in the present study are given in Table 2.

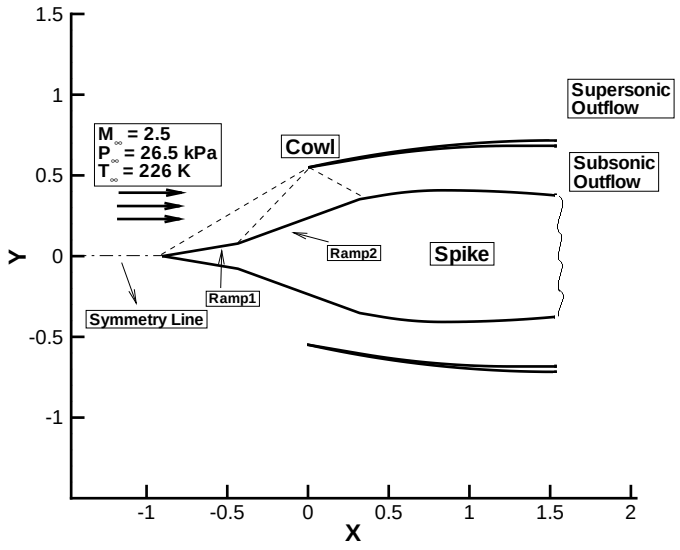

Figure 6: Geometry and boundary conditions for Inlet 3 with combined external and internal compressions (all dimensions in meter).

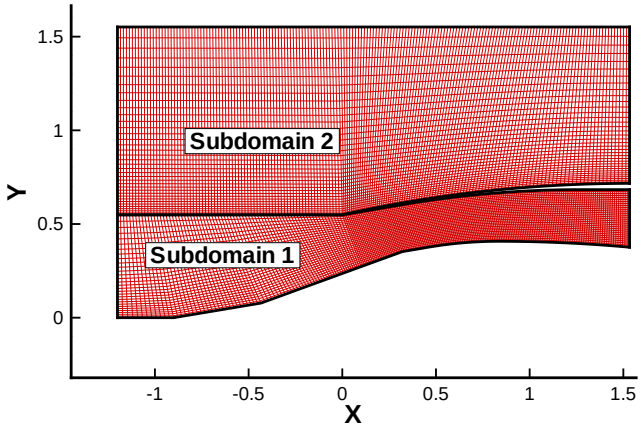

Figure 7: Computational grid and the corresponding subdomains for Inlet 3; Subdomain 1: (229×31), Subdomain 2: (173×37).

Table 2: The grid-independent mesh system used in the present computation.

	Inlet 1	Inlet 2	Inlet 3	Ramjet Engine
Subdomain 1	151×51	349×51	351×51	991×51
Subdomain 2	-	275×51	275×51	451×41

Figure 8: Grid independency test; distribution of pressure coefficient on the spike wall with different grid sizes for Inlet 3. Grid 1: Subdomain 1 (349×71) and Subdomain 2 (275×51); Grid 2: Subdomain 1 (349×51) and Subdomain 2 (275×51).

6.6 The Entire Ramjet

The last case studied in this paper, is the entire ramjet engine with axisymmetric flow and geometry. The engine consists of inlet-diffuser, a subsonic combustion chamber followed by an exhaust nozzle. The flight conditions are Mach $= 3$ at altitude of about $10\ km$ ($p_\infty = 26.5kPa$ and $T_\infty = 226K$). The inlet of the engine is designed based on the Oswatitsch principle described in Sec. 6.2. The designed inlet gives two oblique shocks merging at the engine cowl lip. These shocks are followed by a terminating normal shock located right downstream of the inlet throat. Then, the subsonic flow is delivered to the combustion chamber, where the effect of combustion is simplified by a volumetric heat source (VHS) function that is devised to give a fairly linear distribution of the total temperature along the combustion chamber. The VHS is defined as,

$$VHS = \rho u^* c_p \Delta T_t / L \qquad \text{units: } [Watt/m^3] \tag{22}$$

where u^* is defined as $u^* = max(u, 0)$, in which u is the axial velocity component, ΔT_t is the total temperature rise throughout the combustion chamber (= $T_{t_o} - T_{t_i}$), T_{t_i} and T_{t_o} are respectively the total temperature at the entrance and exit of the combustion chamber, L is the combustion chamber axial length and c_p is the specific heat at constant pressure ($= \gamma R/(\gamma - 1)$). In the following we explain why such a simplified volumetric heat source (VHS), given by Eqn. 22, can properly predict the rate of heat generation through a combustion chamber [22]. It is noted the present computation is aimed only for inviscid cases. But it is shown below that the VHS function in Eqn. 22 is suitable for both viscous and inviscid cases.

The VHS function in Eqn. 22 has the units of W/m^3, and the rate of total heat generation within the combustion chamber (cc) can be determined from:

$$\dot{Q}_{cc} \equiv \int_{cc} VHS \cdot dv = \int_{cc} \left(\rho u^* c_p \frac{\Delta T_t}{L} \right) \cdot dv, \tag{23}$$

where dv is the volume element within the combustion chamber. In a real combustion process, the small values of fluid velocities close to the walls degrade the mixing process between the air and fuel, then a smaller amount of heat release is expected in wall regions. This matter is incorporated in the formula given by Eqn. 22, where the VHS function decreases in the vicinity of walls since u reduces close to the walls in viscous flows due to no-slip conditions at walls. On the other hand, the viscous dissipation term, $\mu\Phi$, appearing in the energy equation:

$$\mu\Phi \equiv \mu\{ \left(\frac{\partial u}{\partial y} + \frac{\partial v}{\partial x} \right)^2 + 2 \left[\left(\frac{\partial u}{\partial x} \right)^2 + \left(\frac{\partial v}{\partial y} \right)^2 \right] + \lambda \left(\frac{\partial u}{\partial x} + \frac{\partial v}{\partial y} \right)^2 \} \qquad \text{units: } [Watt/m^3] \tag{24}$$

increases close to the walls due to large gradients of velocity in the wall regions, where μ is the viscosity, and $\lambda = -(2/3)\mu$. The $\mu\Phi$ term in Eqn. 24 is in fact the rate at which the mechanical work is irreversibly converted to thermal energy due to viscous effects. Hence in fundamental nature, $\mu\Phi$ behaves like a volumetric heat source. The increase in $\mu\Phi$ close to the walls compensates the reduction of VHS in these

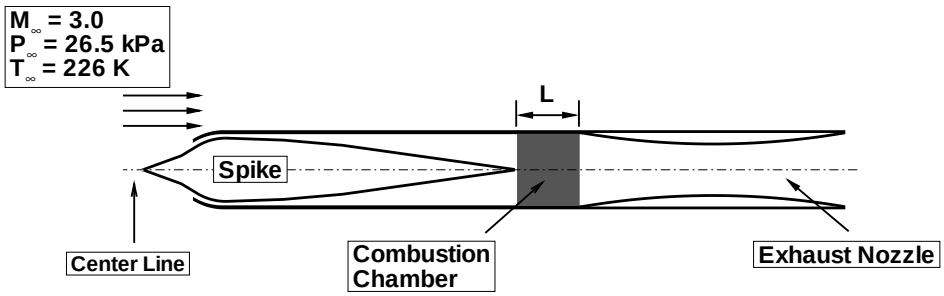

Figure 9: Geometry and boundary conditions for the entire ramjet.

regions. Therefore, in the net, a fairly uniform profile for the rate of heat generation per unit volume (i.e. $VHS + \mu\Phi \approx$ Const.) is achieved in transverse directions for viscous flows. This is in fair agreement with real combustion processes. For the computations of inviscid flows (as is the case in the present study), $\mu\Phi = 0$, and in the absence of viscous effects there is no means to reduce u close to the walls. Therefore, the VHS function fairly gives a uniform profile likewise a real combustion process.

Following the heat injection through the combustion chamber, the pressurized hot gases flow enter to the exhaust nozzle and produce the propulsive thrust.

The geometry and boundary conditions for the ramjet engine are shown in Fig. 9.

6.7 The Performance Analysis

To make performance analysis of the inlets and the entire ramjet, we consider an entire engine. Consider a jet engine surrounded by a control volume around the engine as shown in Fig. 10. Applying the linear momentum equation [23] for the engine:

$$\Sigma\overrightarrow{F} = \frac{\partial}{\partial t}\int_{C.V.} \rho\overrightarrow{V}d\upsilon + \int_{C.S.} \rho\overrightarrow{V}(\overrightarrow{V}\cdot d\overrightarrow{A}). \tag{25}$$

Simplifying this equation along the x-axis for steady state condition, we obtain:

$$F + F_{cowl} + F_f - (P_e - P_\infty)A_e = \dot{m}(V_e - V_\infty), \tag{26}$$

where F is the engine thrust, F_{cowl} is the cowl drag (the engine pressure drag), and F_f is the engine skin friction drag (which is zero in the case of inviscid flow computations). Solving Eqn. 26 for the thrust force, we obtain:

$$F = \underbrace{\dot{m}(V_e - V_\infty)}_{\text{momentum thrust}} + \underbrace{(P_e - P_\infty)A_e}_{\text{pressure thrust}} - F_{cowl} - F_f, \tag{27}$$

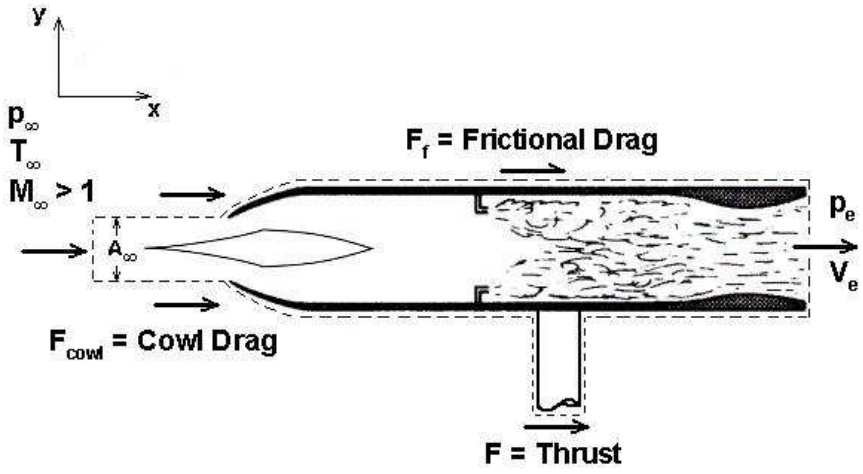

Figure 10: Configuration of a control volume surrounding the ramjet engine.

here $\dot{m}$ is the total mass flow captured by the engine ($= \rho_\infty V_\infty A_\infty$), V_e and V_∞ are respectively the velocity leaving and entering the control volume, and A_e is the nozzle exit area. In Eqn. 27, $\dot{m}(V_e - V_\infty)$ is the momentum thrust, $(P_e - P_\infty)A_e$ is the pressure thrust. In the case of incomplete expansion to ambient pressure, pressure thrust will exist for the price of some loss in momentum thrust.

The most suitable position for the normal shock is right at the inlet throat, as it gives the weakest normal shock. The rise of inlet back pressure (i.e. the pressure at the entrance face of the combustion chamber) pushes the terminating normal shock toward the inlet throat. However, the inlet throat is an unstable position for the normal shock, as slightly excessive inlet back pressure will make the inlet to disgorge the normal shock and give a huge amount of pressure drag (cowl drag). So the inlet back pressure should be properly tuned for the sake of better performance of the inlet. There are two important downstream issues that affect the inlet back pressure, namely the rate of heat release within the combustion chamber ($\dot{Q}_{cc}$ as given by Eqn. 23) and the exhaust nozzle throat area. The increase of $\dot{Q}_{cc}$ and decrease of the exhaust nozzle throat area both raise the inlet back pressure and push the normal shock upstream.

The inlet or the engine cowl drag (as illustrated by F_{cowl} in Fig. 10) is a type of pressure drag and is used to determine the cowl drag coefficient,

$$C_{D_{cowl}} = \frac{F_{cowl}}{\frac{1}{2}\rho_\infty(\gamma R T_\infty)M_\infty^2 A_{Cross}}, \tag{28}$$

here A_{Cross} is the cross sectional area of the cowl-surface perpendicular to the inflow direction. The total pressure recovery of the inlet, η, is defined as the ratio of total pressure at combustion chamber entrance

face, $P_{_{t,f}}$, to that of the free stream, $P_{_{t,\infty}}$:

$$\eta = \frac{P_{_{t,f}}}{P_{_{t,\infty}}}. \tag{29}$$

For the entire engine, the thrust and the energy consumption or conversion values are usually used to represent the engine performance. In specific the thrust, the propulsion efficiency (η_p), the kinetic energy conversion efficiency (η_e), the overall efficiency (η_o) and the thrust specific fuel consumption ($TSFC$) are used for these reasons. These parameters are given as follows:

$$\eta_p = \frac{2}{1 + V_j/V_{_\infty}} \tag{30}$$

$$\eta_e = \frac{\dot{m}(V_j^2 - V_{_\infty}^2)/2}{\dot{m}_f Q_{net,p}} \tag{31}$$

$$\eta_o = \frac{F\, V_{_\infty}}{\dot{m}_f Q_{net,p}} \tag{32}$$

$$TSFC = \frac{\dot{m}_f}{F}\,. \tag{33}$$

Here $V_{_\infty}$ and V_j are the free stream and exhaust nozzle jet velocities, respectively, and $\dot{m}$ is the captured air mass flow rate. $Q_{net,p}$ in Eqns. 31 and 32 is the heating value of a typical hydrocarbon fuel ($= 43100$ $kJ/kg_{_{fuel}}$ [24]) and $\dot{m}_f Q_{net,p}$ is heat rate (kW) of the fuel. For the present computation in which the combustion chamber is modelled by distribution of a volumetric heat source (VHS), an equivalent fuel consumption can be obtained by using Eqn. 23:

$$\dot{m}_f Q_{net,p} = \dot{Q}_{cc} \quad \Rightarrow \quad \dot{m}_f = \frac{\dot{Q}_{cc}}{Q_{net,p}}\,. \tag{34}$$

Using $\dot{m}_f Q_{net,p} = \dot{Q}_{cc}$, Eqn. 32 gives:

$$\eta_o = \frac{F\, V_{_\infty}}{\dot{Q}_{_{cc}}}. \tag{35}$$

As a consequence of inviscid flow assumption, the drag is of pressure-type only. This pressure drag is divided into cowl drag and drag force on the spike. The spike drag in the first observation of Eqn. 27, seems to have no contribution on the calculation of propulsive thrust as it is within inside the control volume of Fig. 10. But in fact the spike effect plays its influence on the internal drag of the engine, and reduces the net momentum thrust (exhaust jet velocity), see Eqn. 27.

Also worth to mention that the captured mass flow ($\dot{m}_f$) is independent of inlet back pressure (i.e. $\dot{Q}_{cc}$ and the exhaust nozzle throat area) as long as the terminating normal shock is remained swallowed by the engine. That is the flow enters to the engine supersonically. Also the cowl drag remains unchanged. These issues are discussed later in Sec. 7.

7 Results and Discussions

The present computations are performed on Inlets 1 – 3, and the entire ramjet geometries described in Section 6. The results are given in this section.

7.1 Inlet 1:

Inlet 1 is a scramjet inlet that is considered for validating the results of the present computations. The flow supersonically enters the computational domain assigned to the inlet and compresses over the 10-degree corner at point C, as shown in Figs. 2 and 11-(a). Fig. 11-(a) also shows the geometry of the inlet, over which the pressure contours and streamlines are superimposed for clarity purposes. All the shocks and expansion fans are clearly illustrated in this figure. Fig. 11-(c) shows the distribution of pressure coefficient C_p for Inlet 1 along the inner part of the top wall, the wall that is shown by red color in Fig. 11-(a). The figure (Fig. 11-(c)) shows the results of the present computations using the 1st, 2nd and 3rd order scheme of Roe, the MacCormack scheme, the Fluent's and the results from the literature [8]. As shown in this figure very good agreement are achieved in all computations, except for the 1st order computations by the Roe scheme. The discrepancy is due to the diffusive behavior of the first order upwind scheme.

The total temperature in the present inviscid flow computation, remains constant throughout the computational domain. This is verified in Fig. 11-(d). The oblique shock, originated from the compression corner at C, say at the bottom wall, is reflected from the opposite wall (the top wall) then impinges on the bottom wall again. On the other hand, the flow expands between the two oblique shocks, when passes over the convex corner that sources a series of expansion fans (waves). As the expansion fans are isentropic, the flow between the two oblique shocks (between the oblique shock originated from the compression corner and the shock reflected from the top wall) remains isentropic, as shown in Fig. 11-(e). Due to the expansion fans, uneven Mach number profiles upstream of each shock is developed. Therefore, each streamline passing through the oblique shock will experience a shock with different strength. This produces a non-isentropic post shock flow as shown in Fig. 11-(e), and according to the Crocco's theorem [19] a rotational flow in this region, as shown in Fig. 11-(f).

7.2 Inlets 2 and 3:

The flows supersonically enter to the computational domains assigned to Inlets 2 and 3 in parallel directions to their symmetry lines. For Inlet 2, the flow passes over three ramps (see Figs. 5 and 12), so three oblique shocks are originated from the lips of the ramps and merge at the engine cowl lip that eliminate any extra reflection from the cowl lip. Then the supersonic flow converts to subsonic flow in Inlet 2, via a terminating normal shock generated by the high value of inlet back pressure imposed at the inlet's exit plane. On the other, in Inlet 3 the flow enters to the internal diffuser after passing through two consecutive external oblique shocks generated by two ramps (see Figs. 6 and 13). These two external oblique shocks are followed by an

internal oblique shock generated by the cowl internal angle in Inlet 3. Then similar to Inlet 2, the flow in Inlet 3 converts to subsonic flow via a terminating normal shock generated by the high value of inlet back pressure.

Fig. 12 shows the contours of Mach number, total temperature, the entropy and velocity vectors in and around the exit plane of Inlet 2, where the entropy at any point w.r.t the inflow entropy is calculated using:

$$s = c_p \ln \frac{T}{T_\infty} - R \ln \frac{p}{p_\infty}\,, \tag{36}$$

in which T_∞ and p_∞ are respectively the static temperature and pressure at the inlet boundary. The line AA' in Fig. 12 corresponds to the cowl lip section at $x = 0$. Also shown in the figure is the pressure coefficient C_p along the spike surface obtained at various inlet back pressures (see Fig. 12-(d)). The subsonic flow leaves Inlet 2 and enters the engine's combustion chamber –not computed here– at Mach number $M_{_{cc}} \approx 0.5$, where $M_{_{cc}}$ is the Mach number at the combustion chamber entrance face. $M_{_{cc}} \approx 0.5$ is usually a suitable speed required by the subsonic combustion chambers [2]. Fig. 12-(e) shows the distribution of Mach number, $M_{_{cc}}$, at the Inlet 2 exit plane (i.e. the combustion chamber entrance face). As shown in this figure, Mach number is just slightly less than 0.5 at the exit plane of the interior part of the inlet, where the flow is delivered to the combustion chamber.

Consider Fig. 6 again that shows the geometry of Inlet 3. Fig. 13 shows the contours of Mach numbers, total temperature, the entropy, and distributions of C_p along the spike surface of Inlet 3 that are obtained at various inlet back pressures. Similar to the AA' line in Fig. 12 the line AA' in Fig. 13 corresponds to the cowl lip section at $x = 0$. As shown in these figures total temperature remains constant throughout the computational domain. Also shown in this figure (see Fig. 13-(e)) is the distribution of Mach number at the interior and exterior portions of Inlet 3 at the exit plane. Likewise Inlet 2, the Mach number at the entrance face of the combustion chamber, $M_{_{cc}}$, is computed ≈ 0.5 (Fig. 13-(e)). The velocity vectors in and around the exit plane of Inlet 3 are also shown in Fig. 13-(f). For comparisons of the results between various numerical solutions for Inlet 3, the flow field computation is performed using the MacCormack scheme as well, and the Mach number contours are shown in Fig. 14. Comparison between Fig. 13-(a) and Fig. 14 shows a unanimous agreement for the Mach number contours. Computations of Inlet 3 are also performed at various back pressures of the inlet to monitor the influences on the positions of normal shock. The results are shown in Fig. 15.

Based on the designs made in this paper, the throat for Inlet 2 is located at the cowl face, whereas in Inlet 3 the supersonic flow continues into the inner part of the diffuser until the flow meets the throat a bit downstream of the intersection of the third oblique shock and the spike surface. Inlet 3 has several advantages from different aspects. It delivers the flow to the combustion chamber at a reasonable level of uniformity. Flow uniformity at the entrance face of the combustion chamber (say uniform profiles of Mach number, pressure and temperature) leads to a more stable combustion processes in the engine combustion chamber. Inlet 3 also has a better efficiency than Inlet 2. Performance analysis of Inlets 2 and 3 are discussed

as follows.

The increase of inlet's back pressure pushes the normal shock toward the inlet throat. Excessive increase of back pressure to values above the on-design value will make the inlet to disgorge the normal shock and give huge amount of pressure drag. On the other a back pressure less than an on-design value will suck the normal shock to deeper sections of the inlet, i.e. into larger sections of the diffuser duct. This will generate a stronger terminating normal shock, increase the inlet losses and degrade the performance of the inlet. Hence there exists an optimized inlet's back pressure the so-called "on-design back pressure". Table 3 summarizes the performances of the inlets for the on-design back pressures (optimized condition) of Inlets 2 and 3.

Inlet 1 is a supersonic inlet and is suitable for scramjet engines. It has the highest efficiency as it lacks any normal shock. On the other hand Inlets 2 and 3 are suitable for ramjet engines. The cowl drag of Inlet 2 (the inlet with external compression only) is a great deal of problematic, as compared with that of Inlet 3 (the inlet with combined internal and external compressions). As noted in Table 3, Inlet 2 has a cowl drag of about 5.5 times larger than that of Inlet 3. This is due to the large cowl lip angle of Inlet 2, which is bent inward as shown in Fig. 6. The inward bent is required to cover the flow-turnings (i.e. the flow diversions from the centerline directions) through three external oblique shocks generated at the ramp lips. It is noted that the cowl drag coefficient ($C_{D_{Cowl}}$) of Inlet 2 is only 3.3 times larger than that of Inlet 3 (as compared to the cowl drag force that was 5.5 times larger). The difference is due the differences in their corresponding $A_{_{Cross}}$. As noted in Table 3, Inlet 3 has a slightly better pressure recovery efficiency (η) as compared to Inlet 2.

7.3 The Entire Ramjet

The last case analyzed here, is the entire ramjet engine in axisymmetric frame. For the geometry and species of the engine refer to Fig. 9 again. With a designated inlet-diffuser for the ramjet a series of parametric studies are performed by varying two parameters and the influences on the performance of the engine are studied. The parameters varied are the rate of heat release through the combustion chamber ($\dot{Q}_{_{cc}}$), and the exhaust nozzle throat diameter ($D_{_{Nozzle}}$).

Fig. 16 shows a sample of computations for the entire ramjet at $\dot{Q}_{_{cc}} = 16.0\ MW$ (ΔT_t = 1105 K) and $D_{_{Nozzle}} = 0.22\ m$. The flight conditions are $M_\infty = 3$, $P_\infty = 26.5\ kPa$, and $T_\infty = 226\ K$. The geometry of the entire ramjet and the contours of Mach number and total temperature in and around the entire engine are shown in Fig. 16. As noted in Fig. 16-(c) total temperature rises just within the combustion chamber, and it remains constant downstream and upstream of the combustion chamber as well as outside the engine. Fig. 17 shows an enlarged view of the Mach number contours in and around the inlet-diffuser of the ramjet. Computations of the entire ramjet at three different levels of $\dot{Q}_{_{cc}}$ are shown in Fig. 18. The figure shows the Mach number contours. As $\dot{Q}_{_{cc}}$ increases the normal shock is pushed upstream. The position of normal shock for each $\dot{Q}_{_{cc}}$ is also illustrated in Fig. 18. Table 4 summarizes the parametric study on the effect of $\dot{Q}_{_{cc}}$ and $D_{_{Nozzle}}$ on the position of inlet-diffuser normal shock. As noted in this table, any decrease in

D_{Nozzle} or any increase in $\dot{Q}_{cc}$ pushes the normal shock in upstream direction. These data are graphically pictured as noted in Fig. 19, for a given D_{Nozzle}. Fig. 20 shows the increase of total temperature along the combustion chamber center line. As expected, a linear profile for the total temperature distribution along the combustion chamber is obtained.

Table 5 summarizes a parametric study on the entire ramjet at various $\dot{Q}_{cc}$. As noted in this table F_{cowl}, $C_{D_{cowl}}$, and $\dot{m}$ do not change with $\dot{Q}_{cc}$, since the normal shock for all of the cases remain swallowed inside the inlet-diffuser of the engine –although it is pushed ahead when $\dot{Q}_{cc}$ increases (see Fig. 18). Therefore, $\dot{Q}_{cc}$ cannot affect the flow configurations outside of the engine. Hence, as long as the normal shock remains inside the inlet, the parameters F_{cowl}, $C_{D_{cowl}}$, and $\dot{m}$ will not change with $\dot{Q}_{cc}$. Similar effects are obtained when D_{Nozzle} changes (these results are not shown here), i.e. as long as the normal shock remains inside the inlet, the parameters F_{cowl}, $C_{D_{cowl}}$, and $\dot{m}$ will not be affected with D_{Nozzle}. The propulsion efficiency η_p reduces with $\dot{Q}_{cc}$ as shown in Table 5, since the jet velocity enhances at higher heat rates of the combustion chamber. On the other hand η_e of the engine increases with $\dot{Q}_{cc}$, since the change in kinetic energy increases with the combustion chamber heat rate. As noted in Table 5 the overall efficiency η_o of the engine gradually increases with $\dot{Q}_{cc}$. This is due to the dominant effect of the engine thrust F in Eqn. 35. The $TSFC$ reduces with $\dot{Q}_{cc}$ since the increase in F is again dominant as compared to the increase in $\dot{m}_{fuel}$ (see Eqn. 33).

8 Conclusions and Future Plans

In this paper three different inlets (Inlets 1 – 3) in planar coordinates and an entire ramjet in axisymmetric frame were numerically studied. The highlights of the present study are given here.

1. Inlet 1, which is suitable for supersonic combustion ramjets, was chosen from the literature and is used to validate the results of the present computations. Very good agreements were achieved in all comparisons.

2. Inlets 2 and 3 were designed in this paper in a way to produce multiple oblique shocks merging at the inlet cowl lip. Inlet 2 gives a solely external compressions via three shocks, while Inlet 3 produces combined external and internal compressions through two and one oblique shocks, respectively. Very large amount of cowl drag is developed in Inlet 2 (about 5.5 times more than that in Inlet 3), which is attributed to large turnings of cowl angle of Inlet 2.

3. The present study has concentrated on the design of supersonic portions of the inlets. To do so we used the Oswatitsch principle. No attempts were made on the design of subsonic portions of the inlet. This task will be done in a separate study.

4. The position of normal shock on the performance of inlet is very important. Generally it is controlled by the inlet back pressure. In the case of entire ramjet, the combustion chamber heat rate ($\dot{Q}_{cc}$) and the exhaust nozzle throat opening (D_{Nozzle}) fix the position of normal shock in ramjet's inlet-diffuser.

5. A simplified but realistic volumetric heat source (VHS) is provided in the present study to simulate the rate of heat release ($\dot{Q}_{cc}$) through the engine combustion chamber.

6. The computations performed here are inviscid and were carried out using (i) the flux difference splitting scheme of Roe (1981) with various orders of accuracy (including the third order upwind biased algorithm), and (ii) the second order predictor-corrector scheme of MacCormack (1969). The commercial software package of the Fluent has also been used in some cases to double check the accuracy of computations. Very good agreements were achieved in all comparisons. Viscous turbulent modelling of the similar problem as performed in the present paper is underway and will come separately.

References

[1] Flack, R.D., “Fundamentals of Jet Propulsion with Applications”, Cambridge Aerospace Series, Cambridge University Press (2005).

[2] Goldsmith, E.L., Seddon, J., “Intake Aerodynamics”, Blackwell Science, Second Edition (1999).

[3] Akbarzadeh, M., Kermani, M.J., “Numerical Computation of Supersonic-Subsonic Ramjet Inlets; a Design Procedure”, 15th Annual (International) Conference on Mechanical Engineering-ISME2007, May 15-17, Amirkabir University of Technology, Tehran, Iran, ISME2007-3056 (2007).

[4] Kumar, A., Singh, D.J., Trexler, C., “Numerical Study of the Effects of Reverse Sweep on Scramjet Inlet Performance”, J. of Propulsion and Power (1992).

[5] Kumar, A., “Numerical Simulation of Scramjet Inlet Flow Fields”, NASA TP-2517, May (1986).

[6] Gokhale, S.S., Kumar, V.R., “Numerical computations of supersonic inlet flow”, Int. J. for Numerical Methods in Fluids, 36:597-617 (2001).

[7] Duncan, B., Thomas, S., “Computational Analysis of Ramjet Engine Inlet Interaction”, SAE, ASME, and ASEE, Joint Propulsion Conference and Exhibit, 28th, Nashville, TN, July 6-8, 12 p (1992).

[8] Hosseini, R., Rahimian, M.H., Mirzaei, M., “Performance of High-Accuracy Schemes in Inviscid Fluxes Calculation”, The Eleventh Annual Conference of the CFD Society of Canada, Vancouver, BC May 28-30 (2003).

[9] Roe, P.L., “Approximate Riemann Solvers, Parameter Vectors and Difference Schemes”, J. of Computational Physics, Vol. 43, pp. 357-372 (1981).

[10] Anderson, J.D., “Computational Fluid Dynamics; The Basics with Applications”, McGraw-Hill (1995).

[11] Hoffmann, K.A., and Chiang, S.T., “Computational Fluid Dynamics for Engineers”, Vol. II, Engineering Education Systems, Wichita, Kansas, USA (1993).

[12] Kermani, M.J., and Plett, E.G., “Roe Scheme in Generalized Coordinates: Part I- Formulations”, AIAA Paper 2001-0086 (2001).

[13] Kermani, M.J., and Plett, E.G., “Roe Scheme in Generalized Coordinates: Part II- Application to Inviscid and viscous Flows, AIAA Paper. 2001-0087 (2001).

[14] van Leer, B., “Towards the Ultimate Conservation Difference Scheme, V, A Second Order Sequel to Godunov’s Method”, J. of Computational Physics, Vol. 32, pp. 110-136 (1979).

[15] Kermani, M.J. and Plett, E.G., “Modified Entropy Correction Formula for the Roe Scheme”, AIAA Paper. 2001-0083 (2001).

[16] Kermani, M.J., “Development and Assessment of Upwind Schemes with Application to Inviscid and Viscous Flows on Structured Meshes”, Ph.D. thesis, Department of Mechanical & Aerospace Engineering, Carleton University, Canada (2001).

[17] MacCormack, R.W., “Numerical Computation of Compressible Viscous Flow”, AA214 Course Notes, Department of Aeronautics and Astronautics, Stanford University, Stanford, CA (1995).

[18] Hirsch, C., “Numerical Computation of Internal and External Flows”, John Wiley & Sons, Vol. 2 (1990).

[19] Anderson, J.D., “Modern compressible flow with historical prospective”, Second Edition, New York, McGraw-Hill (2003).

[20] Hoffmann, K.A., and Chiang, S.T., “Computational Fluid Dynamics for Engineers,” Vol. I, Engineering Education Systems, Wichita, Kansas, USA (1993).

[21] Thompson, J.F., Warsi, Z.U.A., Wayne Mastine, C., “Numerical Grid Generation; Foundations and Applications”, Elsevier Science Publishing Co., Inc. (1985).

[22] Khazaei, H., “Numerical Computation of Flow Field in Ramjets Using a Commercial Software Package”, Undergraduate Project, Amirkabir University of Technology, Tehran, Iran (2006).

[23] White, F.M., “Viscous Fluid Flow”, Second Edition, McGraw-Hill, New York, p. 575 (1991).

[24] Cohen, H., Rogers, G.F.C., Saravanamutto, H.I.H., “Gas Turbine Theory”, Addison Wesley Longman Limited, Fourth Edition (1998).

[25] Zuker, R.D., “Fundamentals of Gas Dynamics”, Second Edition, Wiley Publication (2002).

[26] Gossiping, P., Lesage, F., Champlain Aide., “The Application of Computational Fluid Dynamics (CFD) For the Design of Rectangular Supersonic Intakes”, 6th Annual Conference of the CFD Society of Canada, Quebec City, Canada, June 7-9 (1998).

Table 3: Summary of the computation for Inlets 1–3 for on-design (optimized) condition. Here: **(1)** F_{cowl} is the cowl drag (see Fig. 10 and Eqn. 27), **(2)** $C_{D_{cowl}}$ is the drag coefficient of the cowl (see Eqn. 28), **(3)** The mass flow rate (per unit depth) captured by the inlet.

	F_{cowl} **(1)** (kN)	$C_{D_{Cowl}}$ **(2)**	η (%)	$\dot{m}$ **(3)** $(kg/s/m)$	Comments
Inlet 1	-	-	94.99	246.12	Supersonic outflow, suitable for scramjet
Inlet 2	17.10	0.54	85.64	158.86	Subsonic outflow, suitable for ramjet
Inlet 3	3.11	0.16	89.36	167.48	Subsonic outflow, suitable for ramjet

Table 4: Parametric study on the ramjet performance; the effect of $\dot{Q}_{cc}$ and D_{Nozzle} values on the normal shock location.

	$D_{Nozzle} = 0.20\ m$	$D_{Nozzle} = 0.22\ m$	$D_{Nozzle} = 0.24\ m$
$\dot{Q}_{cc}$ = 7.5 MW ($\Delta T_t = 485K$)	$X_s = 0.61\ m$	$X_s = 0.72\ m$	$X_s = 0.85\ m$
$\dot{Q}_{cc}$ = 10 MW ($\Delta T_t = 690K$)	$X_s = 0.47\ m$	$X_s = 0.67\ m$	$X_s = 0.79\ m$
$\dot{Q}_{cc}$ = 16 MW ($\Delta T_t = 1105K$)	$X_s = 0.37\ m$	$X_s = 0.52\ m$	$X_s = 0.72\ m$

Table 5: Specifications of the ramjet engine at various $\dot{Q}_{cc}$. Here: **(1)** F_{cowl} is the cowl drag (see Fig. 10 and Eqn. 27), **(2)** $C_{D_{cowl}}$ is the drag coefficient of the cowl (see Eqn. 28), **(2)** F_{spike} is the pressure drag over the spike, **(3)** F is the thrust (see Fig. 10 and Eqn. 27), **(4)** $\dot{m}$ is the air mass flow rate captured by the engine, **(5)** η_p is the propulsion efficiency (see Eqn. 30), **(6)** η_e is the kinetic energy conversion efficiency (see Eqn. 31), **(7)** η_o overall efficiency (see Eqn. 32), and **(8)** TSFC is the thrust specific fuel consumption (see Eqn. 33).

$\dot{Q}_{cc}$ (MW)	F_{cowl} **(1)** (kN)	$C_{D_{cowl}}$ **(2)** –	F_{spike} **(3)** (kN)	F **(4)** (kN)	$\dot{m}$ **(5)** (kg/s)	η_p **(6)** (%)	η_e **(7)** (%)	η_o **(8)** (%)	TSFC **(9)** $\frac{kg_{fuel}}{kN \cdot s}$
0	2.65	0.38	3.48	-0.90	15.16	99.19	-	-	-
7.5	2.65	0.38	-9.1	2.50	15.16	92.56	29.51	29.79	70.37
10	2.65	0.38	-11.69	4.13	15.16	88.38	35.62	34.78	60.28
16	2.65	0.38	-15.97	7.06	15.16	81.88	40.60	37.64	55.70

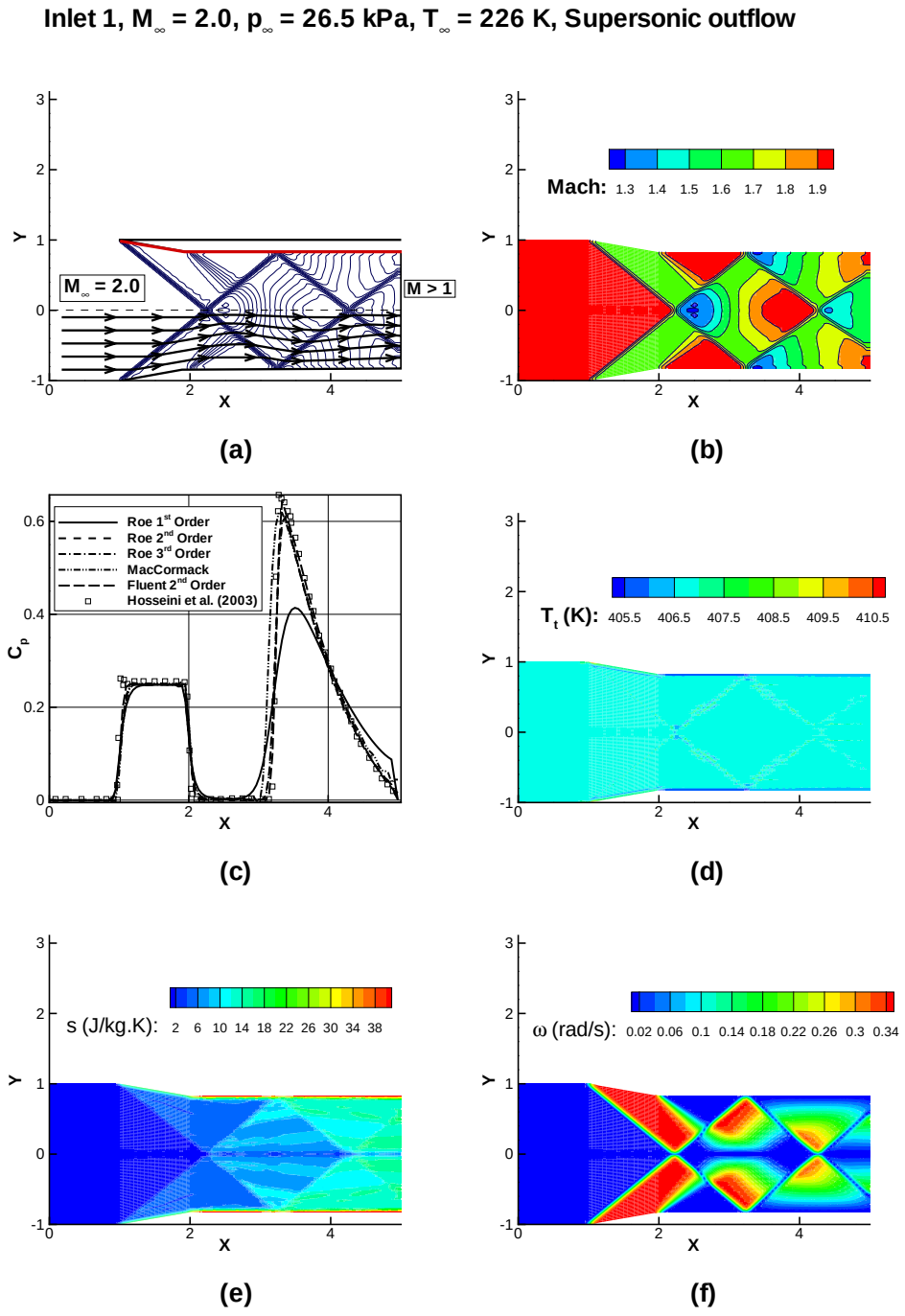

Figure 11: Geometry and boundary conditions for Inlet 1 with supersonic outflow delivered to the combustion chamber; (a) Iso-bar lines with the streamline configuration; (b) Mach number contours; (c) Pressure coefficient along the internal wall; (d) Total temperature contours; (e) The entropy contour; (f) The vorticity contour.

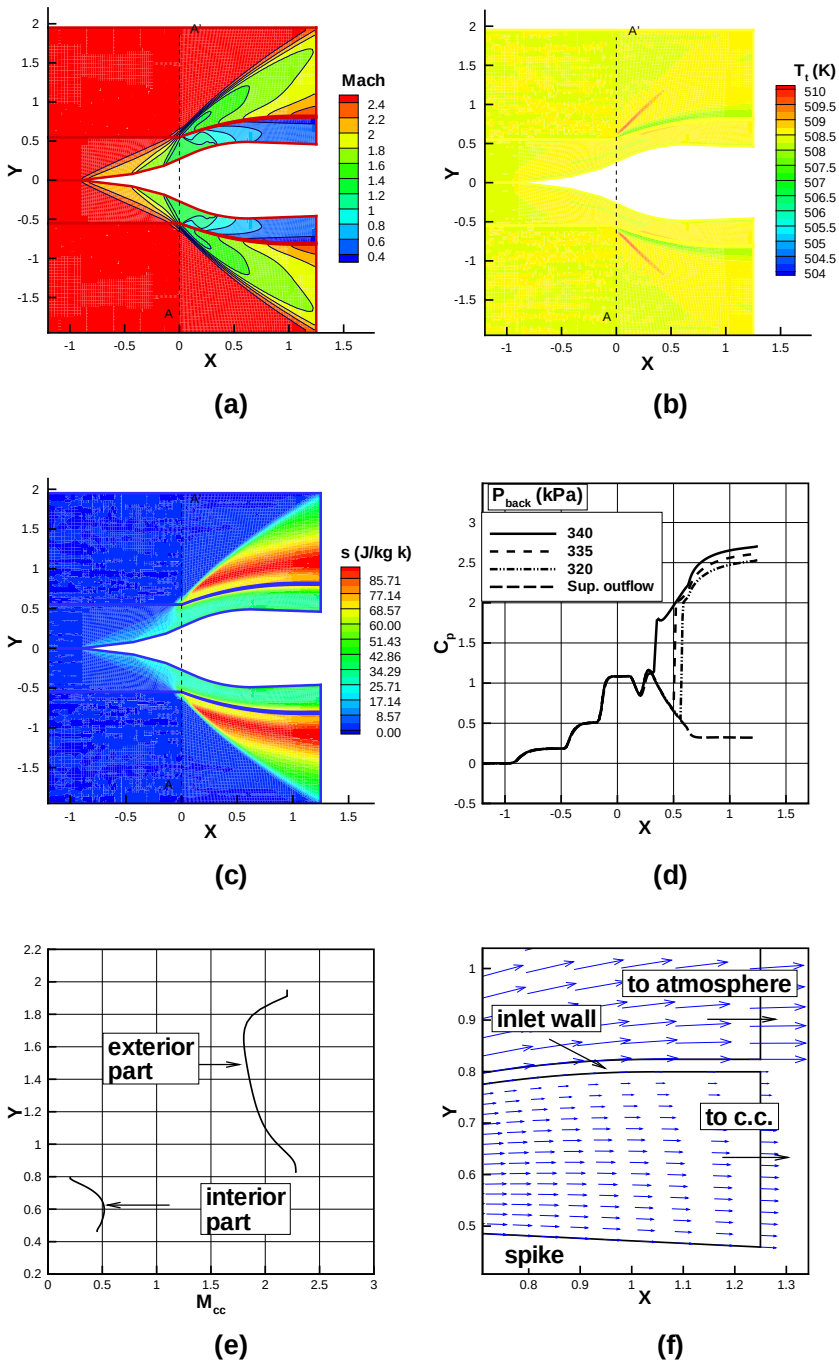

Figure 12: Computation results for Inlet 2; (a) Mach number contours; (b) Total temperature contours; (c) Entropy contours; (d) Pressure coefficient along the spike surface at various inlet back pressures; (e) Profile of Mach numbers at the exit plane of the inlet for both interior and exterior parts; (f) Velocity vectors around the exit plane.

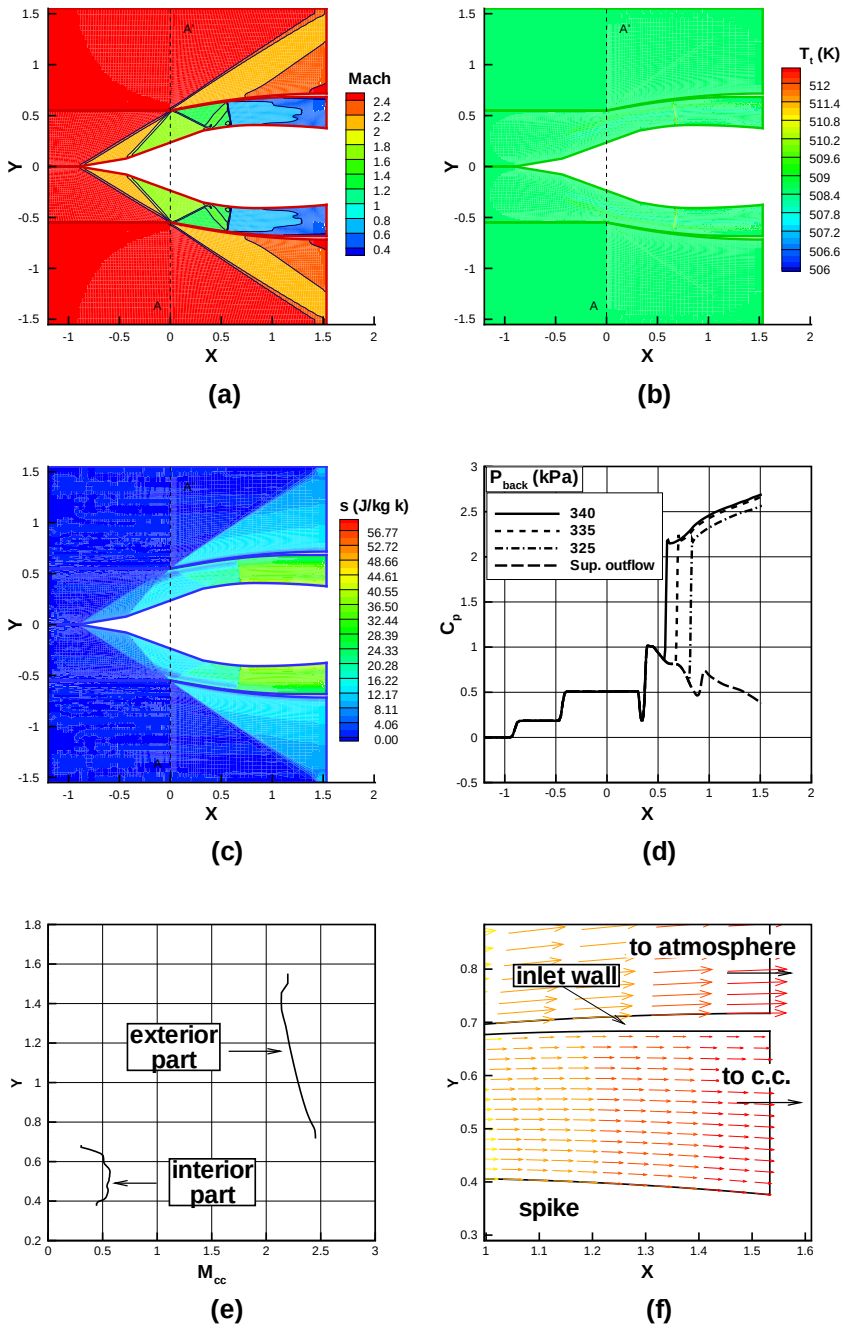

Figure 13: Computation results for Inlet 3; (a) Mach number contours; (b) Total temperature contours; (c) Entropy contours; (d) Pressure coefficient along the spike surface at various inlet back pressures; (e) Profile of Mach numbers at the exit plane of the inlet for both interior and exterior parts; (f) Velocity vectors around the exit plane.

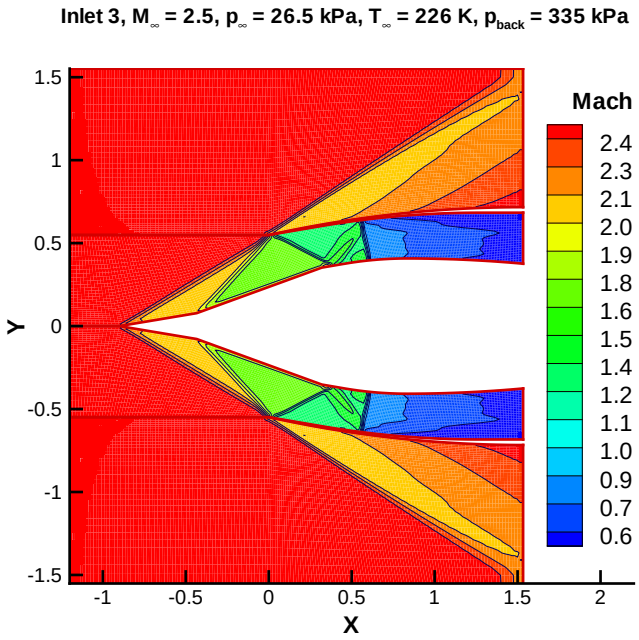

Figure 14: Mach number contours for Inlet 3 in on-design (optimized) back pressure computed by the 2nd order MacCormack scheme.

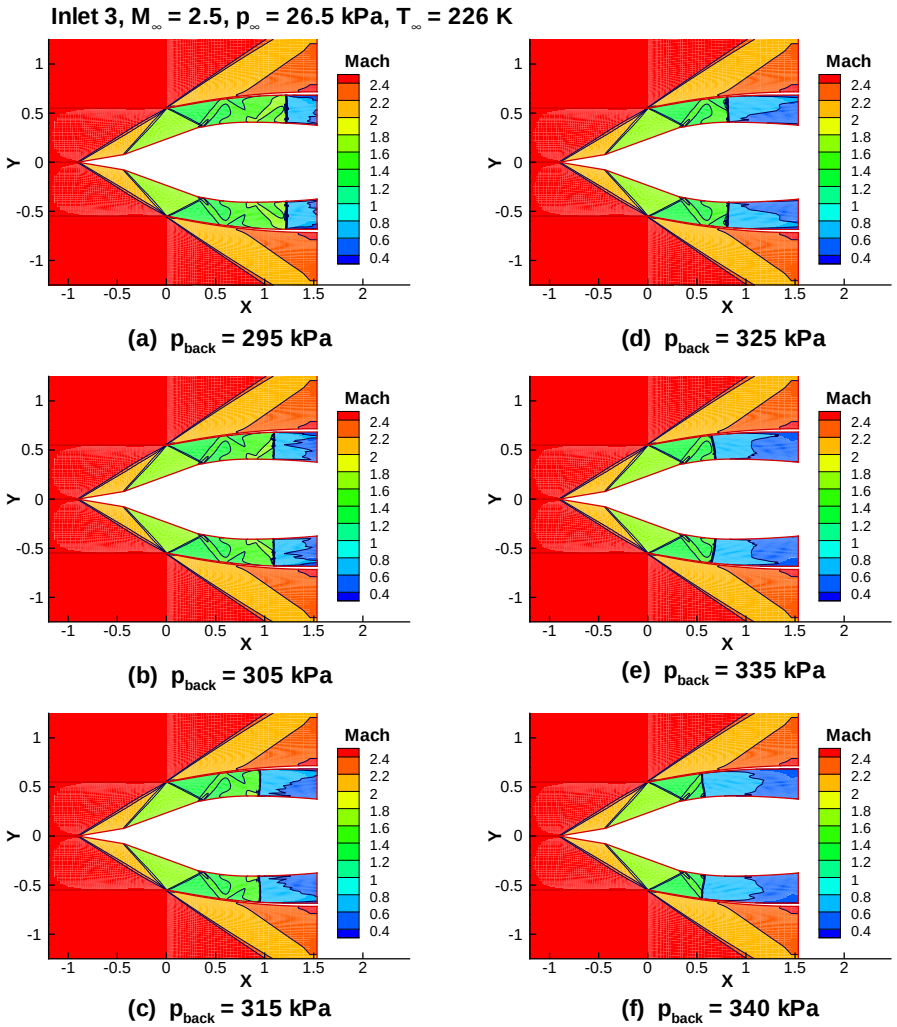

Figure 15: Mach number contours for Inlet 3 at various back pressure values computed by the 3rd order Roe scheme.

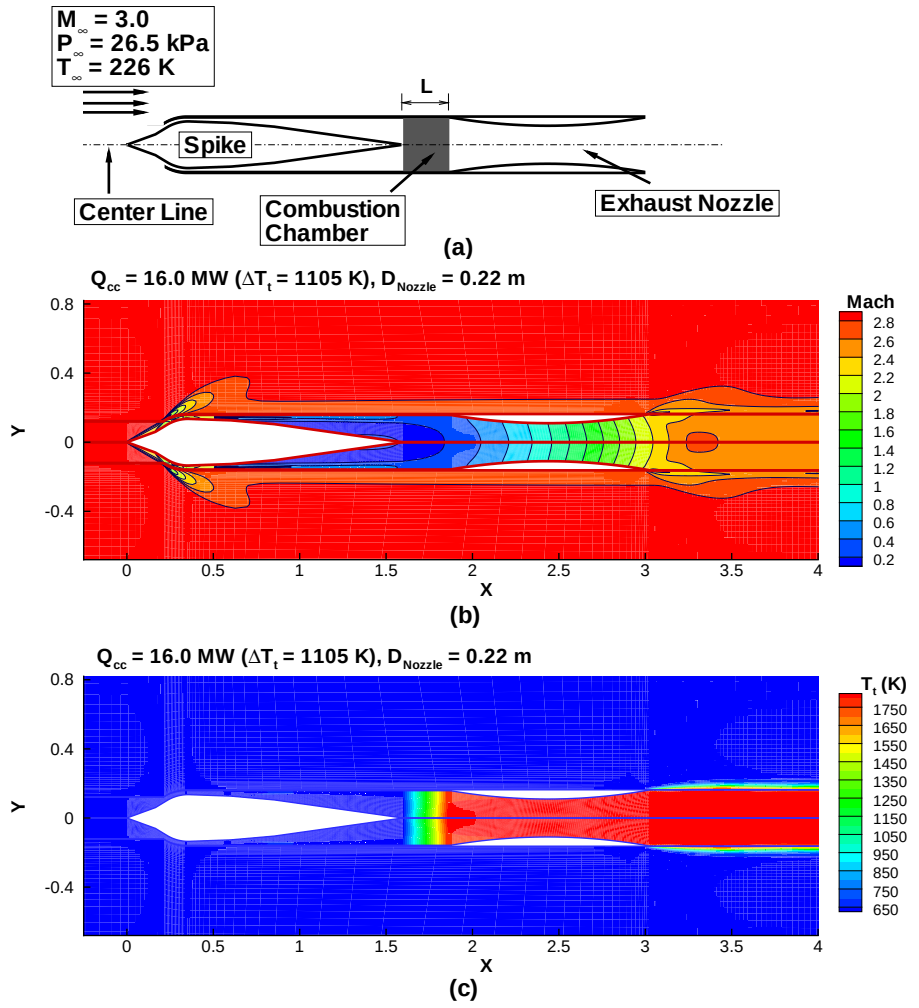

Figure 16: Mach number and total temperature contours for the entire ramjet engine.

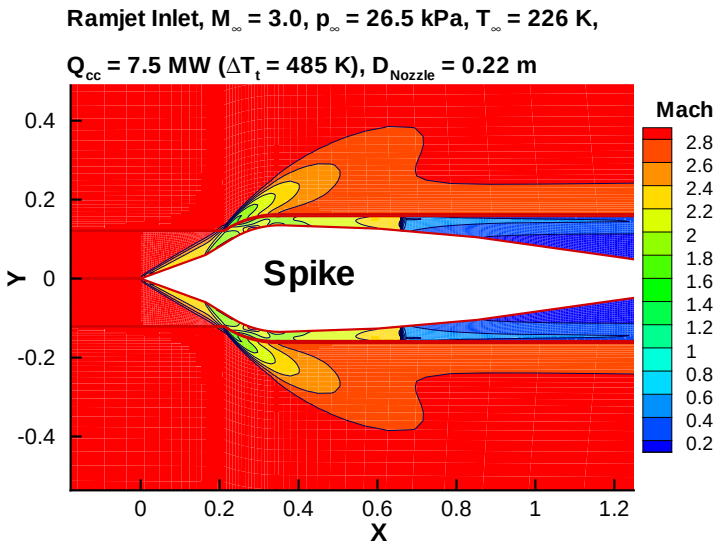

Figure 17: Mach number contours, enlarged in the inlet-diffuser of ramjet.

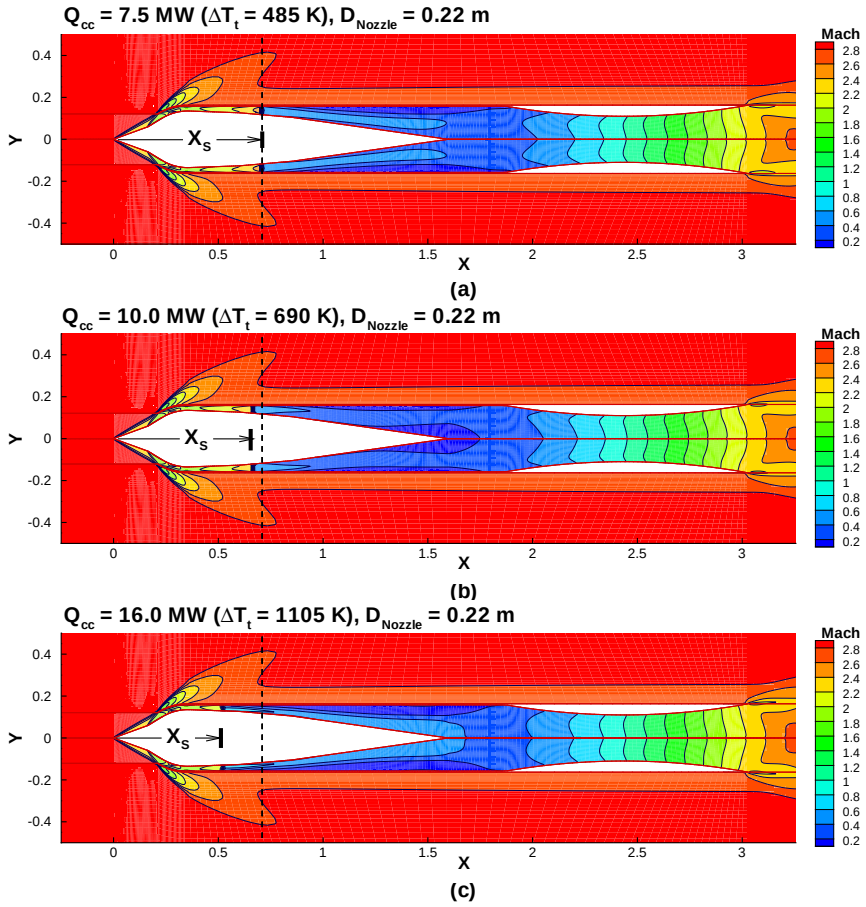

Figure 18: Mach number contours and normal shock movement toward the inlet throat versus different heat source values (a) $\dot{Q}_{cc}$ = 7.5 MW ($\Delta T_t = 485K$) (b) $\dot{Q}_{cc}$ = 10 MW ($\Delta T_t = 690K$) (c) $\dot{Q}_{cc}$ = 16 MW ($\Delta T_t = 1105K$).

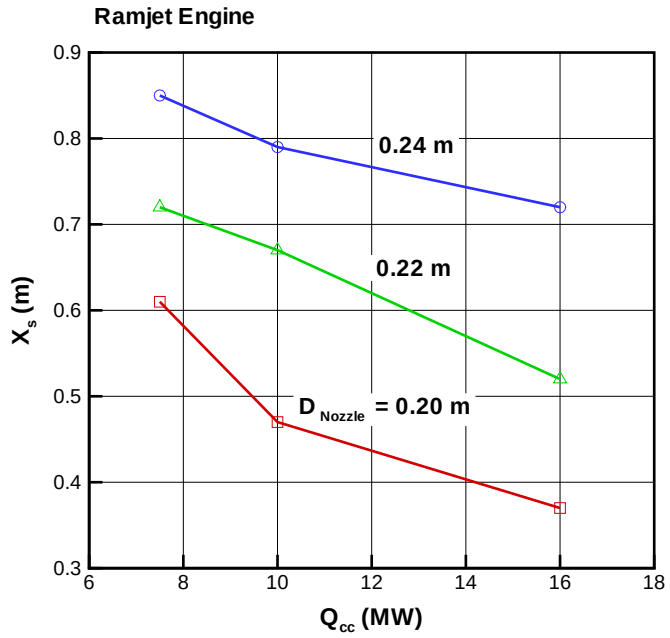

Figure 19: Graphical representation of the data in Table 4; parametric study on the effect of nozzle diameter and heat source level on the position of normal shock.

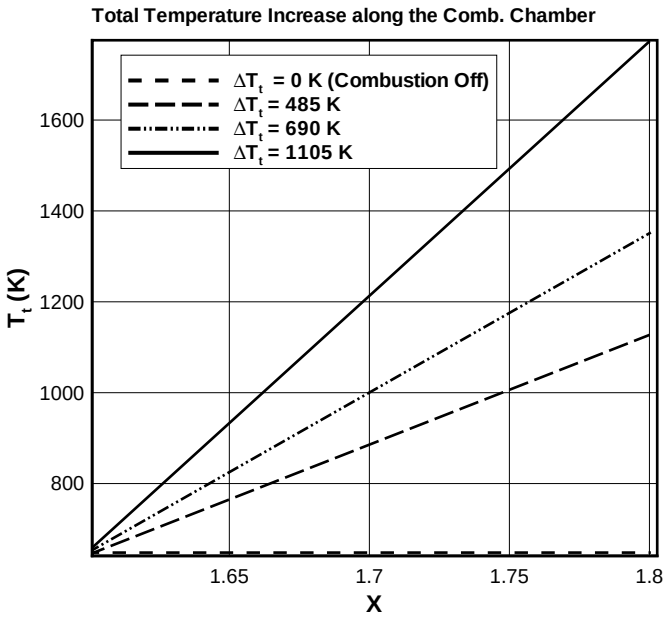

Figure 20: The increase of total temperature along the center line of the ramjet's combustion chamber ($D_{Nozzle} = 0.22\ m$).